

Efficient Implementation of GPR Data Inversion in Case of Spatially Varying Antenna Polarizations

Wang, Jianping; Aubry, Pascal; Yarovoy, Alexander

DOI

[10.1109/TGRS.2017.2779788](https://doi.org/10.1109/TGRS.2017.2779788)

Publication date

2018

Document Version

Accepted author manuscript

Published in

IEEE Transactions on Geoscience and Remote Sensing

Citation (APA)

Wang, J., Aubry, P., & Yarovoy, A. (2018). Efficient Implementation of GPR Data Inversion in Case of Spatially Varying Antenna Polarizations. *IEEE Transactions on Geoscience and Remote Sensing*, 56(4), 2387-2396. <https://doi.org/10.1109/TGRS.2017.2779788>

Important note

To cite this publication, please use the final published version (if applicable). Please check the document version above.

Copyright

Other than for strictly personal use, it is not permitted to download, forward or distribute the text or part of it, without the consent of the author(s) and/or copyright holder(s), unless the work is under an open content license such as Creative Commons.

Takedown policy

Please contact us and provide details if you believe this document breaches copyrights. We will remove access to the work immediately and investigate your claim.

Efficient Implementation of GPR Data Inversion in Case of Spatially Varying Antenna Polarizations

Jianping Wang, Pascal Aubry and Alexander Yarovoy, *Fellow, IEEE*

Abstract—Ground penetrating radar (GPR) imaging from the data acquired with arbitrarily oriented dipole-like antennas is considered. To take into account variations of antenna orientations resulting in spatial rotation of antenna radiation patterns and polarizations of transmitted fields, the full-wave method that accounts for the near-, intermediate- and far-field contributions to the radiation patterns is applied for image reconstruction, which is formulated as a linear inversion problem. Two approaches, namely an interpolation based method and a Nonuniform Fast Fourier transform (NUFFT) based method, are suggested to efficiently implement the full-wave method by computing exact Green's functions. The effectiveness and accuracy of the method proposed have been verified via both numerical simulations and experimental measurements and significant improvement of the reconstructed image quality compared to the traditional scalar-wave based migration algorithms is demonstrated. The results can be directly utilized by forward-looking microwave imaging sensors such as installed at tunnel boring machine or can be used for the observation matrix computation in regularization-based inversion algorithms.

Index Terms—Microwave imaging, Ground Penetrating Radar (GPR), Green's function, Nonuniform Fast Fourier Transform (NUFFT), Radiation pattern, Rotated array.

I. INTRODUCTION

TODAY tunnel boring machine (TBM) has become a very powerful and important piece of equipment for tunnel construction in underground civil engineering projects, for instance, building metro lines and water transportation systems. It substantially improves the working efficiency and reduces human exposure in the hazardous work environment compared to the conventional “hand mining” approach. However, due to lack of adequate geological information in front of a TBM, some potential problems or even risks still exist during tunnel construction. For example, unawareness of brutal change of geological structure may cause a TBM to deviate from the planned construction path. To avoid such problems and risks, a reliable and robust ground prediction system is always required to predict the ground in front of a TBM during its operation.

As a non-destructive test tool, Ground Penetrating Radar (GPR) exploits electromagnetic (EM) waves to investigate subsurface structures and objects, which provides great potential for ground prediction in the TBMs. Although GPR has been broadly used for geophysical investigation and subsurface survey [1], its extension to the TBM application brings some

unique features and thus some new challenges. In the conventional applications, GPR system typically performs measurements along a line or over a two-dimensional (2-D) rectilinear grid on the ground surface while in the TBM application GPR antennas are mounted on the TBM cutter-head and acquire signals during its rotation [2]–[4]. So in essence the GPR signals are acquired with a rotating antenna array over a polar grid, which is named as Radial-Scanned Synthetic Aperture Radar (RadSAR) [5]. However, the rotation of TBM cutter-head constantly changes GPR antenna orientation, i.e., antenna polarization and radiation patterns within the synthesized antenna array, which is distinct from the conventional (synthetic) GPR arrays. As a consequence, this difference makes the scalar wave assumption used for traditional imaging algorithms, for instance, Kirchhoff migration invalid. Thus, their imaging performance is degraded in this circumstance. Although the RadSAR has been discussed for near-field imaging [5] and subsurface object detection [6], however, in both cases the effects of the variation of antenna orientations during the rotation were neglected and EM signals were treated as the scalar wave for imaging.

Due to the vector nature of EM waves, the variation of antenna orientations within the rotating arrays constantly changes the antenna polarizations and then the radiation patterns in space with respect to the scatterers. To circumvent the variation of antenna polarizations within the array aperture, one approach is to retrieve the polarized signals in an aligned polarization basis (e.g., H/V basis) through specifically designed antenna arrays. A novel rotating antenna array was proposed for full-polarimetric imaging in [7], where three co-polarized signals were measured at each spatial position. Through a simple algebraic operation, full-polarized signals are retrieved from the three co-pol measurements at each position. Then the traditional image algorithms can be used for image formation. However, extra antennas are needed in this approach, which is not desirable for the practical GPR systems with limited space for antenna installation such as in TBM applications.

As mentioned above, the variation of antenna orientations causes not only the variation of antenna polarizations but also the variation of radiation patterns with respect to the scatters. So an alternative approach to overcome the impact of the variation of antenna orientations on imaging is to compensate the effects of radiation patterns on the EM signals. In the literature, the effects of antenna radiation patterns have been considered to get quantitatively correct GPR images with the traditional GPR data acquisition schemes [8]–[16]. For example, the far-field radiation pattern derived by Engheta *et al.* [17] has been incorporated in Kirchhoff migration [9] and

This work is partially supported by the NeTTUN project funded by the European Commission within the FP-7 Framework under the Grant 280712.

The authors are with the Faculty of Electrical Engineering, Mathematics and Computer Science (EEMCS), Delft University of Technology, Delft 2628CD, the Netherlands. e-mail: J.Wang-4@tudelft.nl, P.J.Aubry@tudelft.nl, A.Yarovoy@tudelft.nl.

generalized Radon transform [10] for GPR data processing. In [11] and [12], the diffraction tomography is discussed based on the approximated Green's function (GF) in the horizontal wavenumber-frequency (i.e., k - f) domain. In [8], a migration approach is presented by incorporating far-field radiation pattern and Alford rotation to extract the azimuth direction of targets. In [15], a matrix-based inversion approach is proposed in which the co- and cross-polarized GPR data are migrated as a matrix combining the far-field approximation of radiation patterns and their information is merged into one image. By integrating far-field radiation patterns, these approaches provide superior performance compared to the scalar-wave ones. However, the extrema in the far-field radiation patterns generally lead to low image quality, especially for the extended targets illuminated over narrow ranges of incidence angles. To address this problem, the multicomponent imaging approach is further improved by use of full-wave radiation patterns which account for the exact fields, i.e., near-, intermediate- and far-field contributions [16].

Although a fast Fourier transform (FFT)-based method was suggested for exact half-space GFs computation in the k - f domain and the multicomponent migration approach provides the best imaging performance [16], it requires multicomponent GPR data and assumes antenna orientations are consistent within the aperture. Namely, their radiation patterns are linearly translated, i.e., shift-invariant in space. However, this property is spoiled in the case of antennas with spatially varying orientations, for example, rotating antenna arrays in the TBM applications. Thus, it is not straightforwardly applicable in our case.

In this paper, we addressed the problem of GPR imaging by antennas with spatially varying orientations over data acquisition aperture (e.g., rotating antenna arrays), by considering the full-wave radiation patterns through linear inversion. The focus of the paper is the construction of the observation matrix. In the implementation, two methods were suggested to efficiently compute the exact Green's functions of rotated dipole antennas: interpolation based method and Nonuniform FFT (NUFFT) based method. Both methods consider the effects of antenna translation and rotation in space by using the shift and rotation properties of 2-D Fourier transform. By compensating the effects of the variation of antenna orientations, the suggested approach could significantly improve the quality of reconstructed images compared to the traditional ones.

The rest of the paper is organized as follows. In Section II, the linear inversion formulation for the GPR imaging by antennas with spatially varying orientations is presented. Then two approaches to compute exact GFs of rotated antennas are discussed in Section III. Numerical simulations are performed to demonstrate the efficiency and accuracy of the two methods for GF computation as well as the imaging performance of the suggested approach in Section IV. Section V shows experimental results to demonstrate the suggested imaging approach. Finally, some conclusions are drawn in Section VI.

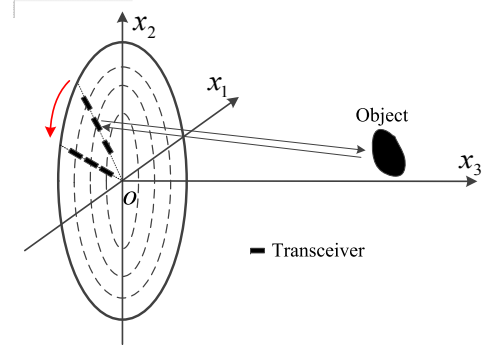


Fig. 1. Geometrical configuration of 3-D imaging with a rotating antenna array. With the rotation of the linear array, the antenna polarizations constantly change.

II. SIGNAL MODEL

Assume the transmit and receive (dipole-like) antennas are placed along a radius of a circular aperture on the x_1ox_2 plane and their orientations are parallel to the radius, as shown in Fig. 1. With the rotation of the circular aperture transmit and receive antenna arrays, the antennas illuminate the scene of interest and the scattered signals are acquired over the space. As a consequence, an equivalent circular antenna array is synthesized. Based on the Born approximation, the scattered electromagnetic signals for a pair of transmitting and receiving antennas can be formulated as [15]

$$\begin{aligned} E_{\alpha\beta}^s(\mathbf{x}^R, \mathbf{x}^T, \omega) &= \int_{V(\mathbf{x}^c)} D_{\alpha\beta}(\mathbf{x}^R, \mathbf{x}^T | \mathbf{x}^c, \omega) \otimes \chi(\mathbf{x}^c) J_{\beta}(\mathbf{x}^T, \omega) dV \\ &= S(\omega) \int_{V(\mathbf{x}^c)} D_{\alpha\beta}(\mathbf{x}^R, \mathbf{x}^T | \mathbf{x}^c, \omega) b_{\beta}(\mathbf{x}^T, \omega) \chi(\mathbf{x}^c) dV \end{aligned} \quad (1)$$

where \otimes denotes the spatial convolution, $D_{\alpha\beta}$ is the wavefield extrapolator that describes the wave propagation of electric field from a β -polarized point source $J_{\beta}(\mathbf{x}^T, \omega)$ at \mathbf{x}^T to a scatterer at \mathbf{x}^c and then to a α -polarized receive antenna at \mathbf{x}^R , $\chi(\mathbf{x}^c) = \hat{\eta} - \eta$ is the contrast function and defined as the difference of the background physical property $\hat{\eta}$ and scatterer's physical property η . Here the electromagnetic physical property η is defined as $\eta = \sigma + j\omega\epsilon$, where σ is the conductivity and ϵ is the permittivity. Moreover, in the last line of (1), it has used the expression for point source $J_{\beta}(\mathbf{x}^T, \omega)$ as a product of the wavelet of the radiated signal $S(\omega)$ and the polarization vector $\mathbf{b}_{\beta}(\mathbf{x}^T, \omega)$: $J_{\beta}(\mathbf{x}^T, \omega) = S(\omega)\mathbf{b}_{\beta}(\mathbf{x}^T, \omega)$. In space, the wavefield extrapolator $D_{\alpha\beta}$ is explicitly represented as an inner product of the Green's functions of transmit and receive antennas

$$D_{\alpha\beta} = \sum_{l=1}^3 G_{\alpha l} G_{l\beta} \quad (2)$$

where $l \in \{1, 2, 3\}$ represents the electric field orthogonal directions. $G_{\alpha l}$ and $G_{l\beta}$ are the Green's functions in the

l direction for α -pol receive and β -pol transmit antennas, respectively. In the discrete form, (1) can be written as

$$E_{\alpha\beta}^s(\mathbf{x}^R, \mathbf{x}^T, \omega) = S(\omega) \cdot \Delta V \cdot \sum_{k=1}^{N_p} D_{\alpha\beta}(\mathbf{x}^T, \mathbf{x}^R | \mathbf{x}_k^c, \omega) \chi(\mathbf{x}_k^c) \quad (3)$$

where N_p is the number of partition cells of the imaging scene and ΔV is the volume of each partition cell. $S(\omega)$ is the spectrum of the wavelet. Considering all the transmit and receive antenna pairs and the discrete frequencies within the signal bandwidth, scattered signals can be represented in a matrix form

$$\mathbf{E}^s = \mathbf{D}_{(N_{tr} \cdot N_f) \times N_p} \cdot \chi(\mathbf{X}^c) \quad (4)$$

where N_{tr} is the number of transmit-receive antenna pairs, N_f is the number of the discrete frequencies within the operational bandwidth, and \mathbf{E}^s is a $N_{tr} \cdot N_f$ column vector formed by all the measurements. In (4), the constant $S(\omega) \cdot \Delta V$ has been normalized with respect to the spectrum of each frequency. $\chi(\mathbf{X}^c)$ is a vector and represents the contrast functions of the pixels

$$\chi(\mathbf{X}^c) = \left[\chi(\mathbf{x}_1^c) \quad \chi(\mathbf{x}_2^c) \quad \cdots \quad \chi(\mathbf{x}_{N_p}^c) \right]^T \quad (5)$$

where superscript \top refers to the matrix transpose operation and $\mathbf{x}_1^c, \mathbf{x}_2^c, \dots, \mathbf{x}_{N_p}^c$ are the positions related to each pixel in the imaging scene. \mathbf{D} is the matrix of the forward wavefield extrapolator, which is represented as

$$\mathbf{D} = [\bar{\mathbf{D}}_1, \bar{\mathbf{D}}_2, \dots, \bar{\mathbf{D}}_{N_{tr}}]^T \quad (6)$$

where $\bar{\mathbf{D}}_s \in \mathbb{C}^{N_p \times N_f}$, $s = 1, 2, \dots, N_{tr}$ and

$$\begin{aligned} \bar{\mathbf{D}}_s &= [\bar{\bar{\mathbf{D}}}(\mathbf{x}_s^{TR}, \omega_1), \bar{\bar{\mathbf{D}}}(\mathbf{x}_s^{TR}, \omega_2), \dots, \bar{\bar{\mathbf{D}}}(\mathbf{x}_s^{TR}, \omega_{N_f})], \\ \bar{\bar{\mathbf{D}}}(\mathbf{x}_s^{TR}, \omega_t) &= \left[D_{\alpha\beta}(\mathbf{x}_s^{TR} | \mathbf{x}_1^c, \omega_t), D_{\alpha\beta}(\mathbf{x}_s^{TR} | \mathbf{x}_2^c, \omega_t), \right. \\ &\quad \left. \dots, D_{\alpha\beta}(\mathbf{x}_s^{TR} | \mathbf{x}_{N_p}^c, \omega_t) \right]^T \end{aligned}$$

where $t = 1, 2, \dots, N_f$, and \mathbf{x}_s^{TR} denotes the positions of the s -th transmit-receive antenna pair, i.e., $(\mathbf{x}^R, \mathbf{x}^T)$.

The objective of imaging process is to retrieve the contrast functions of the targets relative to the background media, which requires to solve the large system of linear equations in (4). The least squares estimation of the contrast functions of the scatters can be represented as

$$\chi(\mathbf{X}^c) = \mathbf{D}^\dagger \cdot \mathbf{E}^s \quad (7)$$

where $\mathbf{D}^\dagger = (\mathbf{D}^H \mathbf{D})^{-1} \mathbf{D}^H$, and the superscript H and $(\cdot)^{-1}$ refer to the Hermitian transpose and the inverse operation of a matrix. As the wavefield extrapolator \mathbf{D} is typically a matrix with dimensions of thousands or even more, the inverse operation of $\mathbf{D}^H \mathbf{D}$ is extremely computationally expensive. To save the computational load, (7) can be rearranged as

$$\mathbf{D}^H \mathbf{D} \chi = \mathbf{D}^H \mathbf{E}^s \quad (8)$$

Then some iterative approaches can be used to solve (8). In this paper, we used the BiConjugate Gradient Stabilized method

(BiCGStab) [18]. Here, as long as the matrix of forward wavefield extrapolator \mathbf{D} is computed, (8) can be solved to reconstruct the contrast functions of scatterers. Therefore, the other major computational effort has to be spent to compute the Green's functions for each transmit-receive antenna pair at each frequency with respect to the imaging region. Considering the constant variation of antenna polarizations within the aperture, two approaches are suggested to compute the exact Green's functions in the space-frequency and wavenumber-frequency domain, respectively, in the following.

III. COMPUTATION OF x - f DOMAIN EXACT GREEN'S FUNCTIONS OF ROTATED ANTENNAS

The exact k - f domain Green's functions for the dipole antennas placed on the surface of homogeneous ground (i.e., $x_1 o x_2$ plane) can be denoted by [16]

$$\begin{pmatrix} \tilde{G}_{11} & \tilde{G}_{12} \\ \tilde{G}_{21} & \tilde{G}_{22} \\ \tilde{G}_{31} & \tilde{G}_{32} \end{pmatrix} = -\zeta \begin{pmatrix} k_1^2 V + U & k_1 k_2 V \\ k_1 k_2 V & k_2^2 V + U \\ -jk_1 \Gamma_0 V & -jk_2 \Gamma_0 V \end{pmatrix} \quad (9)$$

where

$$U = \frac{\exp(-\Gamma_1 x_3)}{\Gamma_0 + \Gamma_1}, \quad V = \frac{\exp(-\Gamma_1 x_3)}{\gamma_1^2 \Gamma_0 + \gamma_0^2 \Gamma_1} \quad (10)$$

$$\Gamma_i = \sqrt{\gamma_i^2 + k_1^2 + k_2^2} \quad (11)$$

and

$\gamma_i^2 = \eta_i \zeta$ complex propagation constants for air ($i = 0$) and the subsurface ($i = 1$);

$\eta_i = \sigma_i + j\omega\epsilon_i$ electric material parameters for conductivities σ_i and permittivities ϵ_i ;

$\zeta = j\omega\mu_0$ magnetic material parameter with permeability μ_0 ;

k_1, k_2 wavenumbers on the ground plane;

$\omega = 2\pi f$ angular frequency.

In (9), “ $\tilde{\cdot}$ ” above G is used to indicate the wavenumber-frequency domain, which will also be used in the following. Taking inverse Fourier transform (IFT) of the Green's functions in (9) with respect to k_1 and k_2 , their counterparts in the space-frequency (i.e., x - f) domain are obtained

$$\begin{pmatrix} G_{11}(x_1, x_2, \omega) & G_{12}(x_1, x_2, \omega) \\ G_{21}(x_1, x_2, \omega) & G_{22}(x_1, x_2, \omega) \\ G_{31}(x_1, x_2, \omega) & G_{32}(x_1, x_2, \omega) \end{pmatrix}.$$

Note (9) gives the exact Green's functions of an antenna at $(0, 0, 0)$ along the x_1 or x_2 axis. For shifted antennas in the traditional arrays, their Green's functions are obtained through the linear translation in space according to the space shift-invariant property. However, for the rotated antenna arrays, the antennas within the aperture are not only linear translated but also rotated. To obtain the corresponding Green's functions, both translation and rotation operations are needed in the x - f domain. In what follows, two methods are suggested to compute the exact Green's functions of rotated antennas.

A. Computation of Green's functions via Interpolation

For image reconstruction, Green's functions over a rectilinear grid in the x_1 - x_2 - x_3 coordinate system are required. Let us assume the imaging grid in space at a certain depth is defined as

$$I = \left\{ (x_{1p}, x_{2q}) \left| \begin{array}{l} x_{1p} = p\Delta x_1, x_{2q} = q\Delta x_2 \\ p = 0, 1, \dots, N_{x_1} - 1; \\ q = 0, 1, \dots, N_{x_2} - 1 \end{array} \right. \right\} \quad (12)$$

where Δx_1 , Δx_2 are the grid intervals along the x_1 and x_2 axes and N_{x_1} , N_{x_2} are the associated numbers of sample points. Assume a dipole antenna is placed at $(x_1^a, x_2^a, 0)$ with an orientation angle of θ with respect to the x_1 axis and denote the antenna orientation and its normal direction as x_θ and x_{θ_\perp} . For the convenience of discussion in the following, we define a "local" coordinate system x_θ - x_{θ_\perp} - x_3 with the origin at $(x_1^a, x_2^a, 0)$ and denote k_θ and k_{θ_\perp} as the Fourier counterparts of x_θ and x_{θ_\perp} . Then in the "local" k_θ - k_{θ_\perp} - f domain, the Green's functions $\tilde{G}_{l\theta}^a(k_\theta, k_{\theta_\perp}, \omega)$, where the superscript a indicates the corresponding spatial center of the GF is at the antenna position and the subscript θ is the explicit substitution of α (or β) in (2) and represents the antenna orientation, on a grid Φ can be directly calculated via (9), and the grid Φ is defined as

$$\Phi = \left\{ (k_{\theta_m}, k_{\theta_\perp n}) \left| \begin{array}{l} k_{\theta_m} = m\Delta k_\theta; \\ k_{\theta_\perp n} = n\Delta k_{\theta_\perp}; \\ m = 0, 1, \dots, L_{k_\theta} - 1 \\ n = 0, 1, \dots, L_{k_{\theta_\perp}} - 1 \end{array} \right. \right\} \quad (13)$$

where the sampling intervals Δk_θ and Δk_{θ_\perp} are determined by the field of view of the imaging scene according to the Nyquist criterion, and L_{k_θ} and $L_{k_{\theta_\perp}}$ are, respectively, the numbers of sample points along the k_θ and k_{θ_\perp} directions. In [16], it suggests that in practical implementation the wavenumber sampling grid should be 4 ~ 16 times over sampled compared to the Nyquist sampling requirements in order to get accurate radiation properties of antennas, especially for the near-field. Taking the IFFT of $\tilde{G}_{l\theta}^a(k_\theta, k_{\theta_\perp}, \omega)$ with respect to k_θ and k_{θ_\perp} , the Green's functions $G_{l\theta}^a(x_\theta, x_{\theta_\perp}, \omega)$ in the x_θ - x_{θ_\perp} - f domain are obtained.

To get the Green's functions $G_{l\theta}$ for imaging, a mapping of the Green's functions from the x_θ - x_{θ_\perp} grid to the imaging grid I has to be made, including both linear translation and rotation operation in space. Explicitly, this mapping can be written as

$$G_{l\theta}(x_1, x_2, \omega; x_1^a, x_2^a, \theta) = G_{l\theta}^a(\tilde{x}_\theta, \tilde{x}_{\theta_\perp}, \omega) \quad (14)$$

where

$$\begin{aligned} \tilde{x}_\theta &= (x_1 - x_1^a) \cos \theta + (x_2 - x_2^a) \sin \theta \\ \tilde{x}_{\theta_\perp} &= -(x_1 - x_1^a) \sin \theta + (x_2 - x_2^a) \cos \theta \end{aligned}$$

From (14), we can see that Green's functions over a new grid $(\tilde{x}_\theta, \tilde{x}_{\theta_\perp})$ in x_θ - x_{θ_\perp} coordinate system are needed to get the corresponding values on the grid I . As the new grid $(\tilde{x}_\theta, \tilde{x}_{\theta_\perp})$ is generally different from that determined by the Fourier grid Φ , so two-dimensional (2-D) interpolation is

required to implement the mapping from a rectilinear grid $(x_\theta, x_{\theta_\perp})$ to the rectilinear grid I . Many interpolation methods, for example, nearest, cubic, spline, are applicable for this operation. Considering both accuracy and efficiency, spline interpolation is used in this paper.

In addition, we have to say that instead of taking the interpolation in x - f domain, the Green's function $G_{l\theta}(x_1, x_2, \omega; x_1^a, x_2^a, \theta)$ can also be obtained via direct Fourier summation of $\tilde{G}_{l\theta}^a(k_\theta, k_{\theta_\perp}, \omega)$, which is expressed as

$$\begin{aligned} &G_{l\theta}(x_1, x_2, \omega; x_1^a, x_2^a, \theta) \\ &= \sum_{m=0}^{L_{k_\theta}-1} \sum_{n=0}^{L_{k_{\theta_\perp}}-1} \tilde{G}_{l\theta}^a(k_{\theta_m}, k_{\theta_\perp n}, \omega) \\ &\quad \cdot \exp\{-jk_{\theta_m} \cdot [(x_1 - x_1^a) \cos \theta + (x_2 - x_2^a) \sin \theta]\} \\ &\quad \cdot \exp\{-jk_{\theta_\perp n} \cdot [-(x_1 - x_1^a) \sin \theta + (x_2 - x_2^a) \cos \theta]\} \end{aligned} \quad (15)$$

The computation of Green's functions via (15) is referred as direct summation method in the following text.

B. Computation of Green's functions with NUFFT

In this section, we propose to take advantage of Nonuniform Fast Fourier Transform (NUFFT) [19] to accelerate the computation of x - f domain Green's functions.

Linear translation and rotation operations in space are required to obtain the Green's functions in the previous section. Actually, these operations can also be efficiently implemented in the wavenumber domain. According to the properties of two-dimensional (2-D) Fourier transform, the operations in (14) can be represented in the wavenumber domain as

$$\begin{aligned} &\tilde{G}_{l\theta}(k_1, k_2, \omega; x_1^a, x_2^a, \theta) \\ &= \mathcal{F}_{2D}[G_{l\theta}(x_1, x_2, \omega; x_1^a, x_2^a, \theta)] \\ &= \tilde{G}_{l\theta}^a(k_1 \cos \theta + k_2 \sin \theta, -k_1 \sin \theta + k_2 \cos \theta, \omega) \\ &\quad \cdot \exp\{-j[(k_1 \cos \theta + k_2 \sin \theta) x_1^a \\ &\quad + (k_2 \cos \theta - k_1 \sin \theta) x_2^a]\} \end{aligned} \quad (16)$$

where $\tilde{G}_{l\theta}$ is the counterpart of $G_{l\theta}$ in the k - f domain in the (k_1, k_2) coordinate system, and \mathcal{F}_{2D} is the 2-D Fourier transform operator. In (16), the exponential terms describe the translation operation in space while the trigonometric terms are related to the rotation.

Then to get the Green's functions $G_{l\theta}$ of a rotated antenna over the grid I , the Green's functions $\tilde{G}_{l\theta}$ should be computed over a rectilinear grid on k_1 - k_2 plane. According to (16), the corresponding values $\tilde{G}_{l\theta}^a$ have to be calculated on an irregular grid $(k_1 \cos \theta + k_2 \sin \theta, -k_1 \sin \theta + k_2 \cos \theta)$, which can be obtained directly via (9). However, due to the varied antenna orientation angles, the grid points $(k_1 \cos \theta + k_2 \sin \theta, -k_1 \sin \theta + k_2 \cos \theta)$ change for antennas at different azimuthal positions. Hence the point-by-point computation of Green's function has to be performed for every antenna with different orientations. This is even more computationally expensive than the interpolation-based method.

One alternative approach to address this problem is to exploit the similar idea as the Stolt interpolation for one-dimensional mapping. Firstly, equations (9), (10), and (11) are

used to compute the Green's functions $\tilde{G}_{l\theta}^a$ in the k - f domain over the grid Φ . After the k - f domain Green's functions are obtained point by point, then they can be used to calculate the x - f domain Green's functions for every antenna within the aperture. For an antenna at $(x_1^a, x_2^a, 0)$ with orientation of angle θ with respect to the x_1 axis, the pre-computed Green's functions over the regular grid in the $(k_\theta, k_{\theta_\perp})$ basis that is rotated by θ in counter-clockwise with respect to the (k_1, k_2) basis are mapped onto the grid

$$\Phi' = \left\{ (k_1, k_2) \begin{cases} k_1 = k_{\theta_m} \cos \theta + k_{\theta_\perp n} \sin \theta; \\ k_2 = -k_{\theta_m} \sin \theta + k_{\theta_\perp n} \cos \theta; \\ (k_{\theta_m}, k_{\theta_\perp n}) \in \Phi \end{cases} \right\} \quad (17)$$

in the (k_1, k_2) basis. Obviously, after the rotation mapping from $(k_{\theta_m}, k_{\theta_\perp n}) \rightarrow (k_1, k_2)$, the sample points are located on a skewed grid in the (k_1, k_2) basis.

So the problem can be restated as: *Using the pre-calculated k - f domain Green's functions over the irregular grid Φ' to reconstruct their counterparts in the x - f domain over the rectilinear grid I .* Apparently, it is a typical nonuniform Fourier transform problem from nonuniform samples in the k - f domain to the uniform grid in the x - f domain. So we can take advantage of NUFFT to efficiently implement it [19]. To compute the Green's functions in a 3-D volume, the wavefield calculated in a ground plane can be extrapolated to different depth via the derived k - f domain relation [20]

$$\tilde{G}_{l\theta} \left(k_1, k_2, \omega, x_3^{(n)} \right) = \tilde{G}_{l\theta} \left(k_1, k_2, \omega, x_3^{(0)} \right) \times \exp \left\{ -\Gamma_1 \left(x_3^{(n)} - x_3^{(0)} \right) \right\} \quad (18)$$

where $x_3^{(0)}$ is the initial depth of the electric fields computed directly and $x_3^{(n)}$ is the depth of the extrapolated electric fields. As the exponential term in (18) is rotationally symmetric around the origin on the k_1 - k_2 plane, so it is directly applicable to extrapolate the wavefield to different depths for antennas with various orientations on the x_1 - x_2 plane.

C. Sampling Criteria

In all the three methods, the uniform sampling of $\tilde{G}_{l\theta}^a$ is required for the x - f domain GFs computation. The wavenumber domain sampling spacings can be taken as [16]

$$\Delta k_i = \frac{2\pi}{p \cdot X_i} \quad (19)$$

where p is the oversampling factor, X_i is the dimension of the imaging scene in the x_i direction and $i \in \{\theta, \theta_\perp\}$. As the k - f domain Green's functions $\tilde{G}_{l\theta}^a$ are calculated only once for all the antennas within the aperture, then X_i s usually choose the value of the maximum cross-range dimension of the imaging scene. Considering the computational accuracy of IFFT-derived Green's functions in the x - f domain, p could empirically take a value of 4 to 16. Moreover, we have to mention that when the interpolation based method is used to compute the Green's functions, a large enough value should be chosen for p so that the support region of the computed Green's functions always covers the desired imaging area in

TABLE I
COMPARISON OF THREE METHODS FOR x - f DOMAIN GREEN'S FUNCTION COMPUTATION

Method		Direct-sum	Interp	NUFFT
Time [s]		1042.64	4.042	0.553
L_2 Error	G_{11}	-	1.269e-8	1.373e-14
	G_{21}	-	2.034e-8	1.524e-14
	G_{31}	-	2.358e-8	1.827e-14
L_∞ Error	G_{11}	-	1.033e-4	1.255e-7
	G_{21}	-	1.500e-4	1.644e-7
	G_{31}	-	1.655e-4	1.683e-7

the spatial domain even after translation with respect to the most remote antenna from the origin.

Here it should be mentioned that in this paper we use elementary dipole sources and ideal receivers for the above discussion considering two aspects: (1) in practice, dipole-like antennas, e.g., loaded dipoles or bow-tie antennas, are widely used in GPR system. In these circumstances, the elementary dipole source could be a good approximation model for the observation matrix construction, which will be verified below through both numerical simulations and experimental measurements; (2) for more complex antennas, theoretically we can use the superposition principle to get the corresponding Green's functions.

IV. SIMULATION

A. Green's Function Computation

In this section, Green's function computation methods are examined via numerical simulations. In this simulation, the operational frequency was 200MHz and the relative permittivity of soil medium was 9. Dipole antennas were placed on the x_1 - x_2 plane and their orientation angles were defined as the angles from the x_1 -axis to antenna axes. The x_3 -axis points downward, forming a right-hand coordinate system with the x_1 - and x_2 -axes. At first, Green's functions for a dipole antenna at the origin along the x_1 axis were calculated in the approach presented in [16]. Then Green's functions for a linearly translated and rotated antenna were computed by the interpolation based method and NUFFT based method discussed in the previous section. In order to get accurate x - f domain Green's functions, four times oversampling in the k - f domain computation was taken for all simulations and the computation accuracy of NUFFT was set to be $1e-5$. The computation results are illustrated in Fig. 2. Green's functions for a dipole antenna located at the origin at the depth of 0.6m are shown in Fig. 2 (a)–(c) while the Green's functions for a dipole antenna at (1, 1, 0)m with the orientation angle of 45° are displayed in 2 (d)–(l). The Green's functions obtained with the interpolation method and NUFFT based method are presented in Fig. 2 (g), (h), (i) and Fig. 2 (j), (k), (l). As a reference, the results computed by direct summation are shown in Fig. 2 (d), (e) and (f). According to 2 (d)–(l), both the interpolation based method and NUFFT based method obtain the visually equal results as those of direct summation.

The efficiency and accuracy of both methods were also compared quantitatively and the results are listed in Table. I.

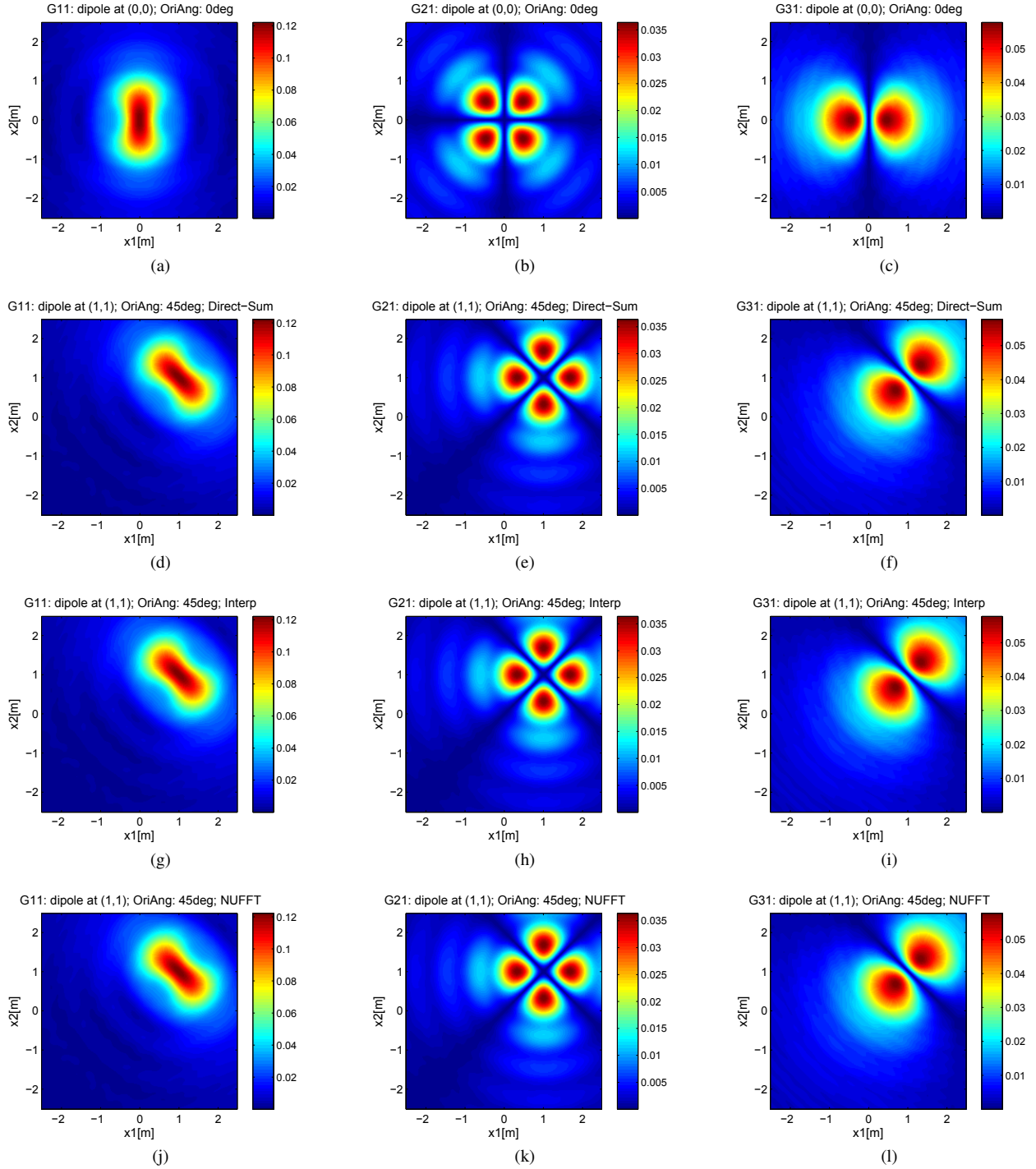


Fig. 2. Green's functions for dipole antennas located at $(0, 0, 0)$ with orientation along x_1 -axis [(a)–(c)] and at $(1, 0, 1)$ m with orientation of 45° from the x_1 -axis [(d)–(l)] at the depth of 0.6m. (d)–(f) are computed by direct summation; (g)–(i) are by the interpolation based method; and (j)–(l) are obtained with the NUFFT based method. The antennas are placed on the ground surface (x_1 or x_2 plane). The operational frequency is 200MHz and the relative permittivity of soil $\epsilon = 9$.

The accuracy is indicated by relative L_2 error and relative L_∞ error. The relative L_2 error is defined by the norm of the differences between the computed Green's function with suggested method and the reference Green's function divided by the norm of the reference Green's function. The relative L_∞ is defined by the maximum of the differences between the computed Green's function with suggested method and

the reference Green's function divided by the norm of the reference Green's function. In terms of both relative L_2 error and relative L_∞ error, the NUFFT based method for Green's function computation achieves much higher accuracy than that of the interpolation based one. Although both suggested methods significantly improve the computation efficiency compared to the direct summation method, the NUFFT based method

TABLE II
PARAMETERS FOR GPR SIMULATION WITH DIELECTRIC CYLINDERS IN THE SOIL

Parameter	Value
Wavelet	Ricker [900 MHz]
Radial sampling interval	5 cm
Azimuthal sampling interval	3°
Radius of circular antenna aperture	0.5 m
Permittivity of background soil	9.0
Soil conductivity	0.01 S/m
Permittivity of dielectric cylinders	5.0
Conductivity of dielectric cylinders	0.05 S/m
Depth of the cavity	0.4 m

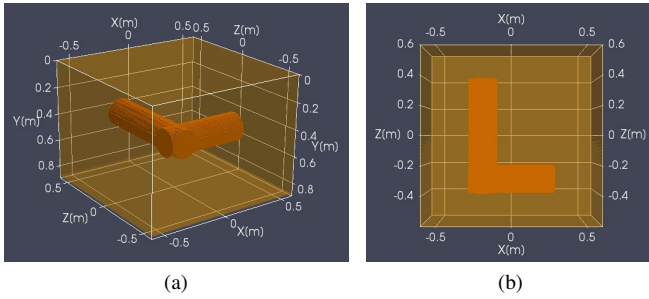


Fig. 3. Geometrical configuration of dielectric cylinders in the soil. (a) is the 3-D geometrical configuration and (b) is its top view along the positive y direction.

is still more than 7 times faster than the interpolation based method for a 250×250 points x - f domain Green's function computation.

B. Imaging with rotating antenna array

To demonstrate the imaging performance of the proposed approach, numerical simulations were performed for dielectric cylinders buried in the soil. GPR data was synthesized with `gprMax` software, which uses the Finite-Difference Time-Domain (FDTD) method to simulate the electromagnetic wave propagation [21]. The geometrical configuration for the simulation is shown in Fig. 3. Two cylinders of radius 10cm were buried at the depth of 0.4m and they were joined at one end (as shown in Fig. 3(a)). The relative permittivity of the cylinders is 5.0 and their conductivity is 0.05S/m. Meanwhile, the permittivity and conductivity of background soil are 9.0 and 0.01S/m, respectively. The elementary dipole antennas were placed on the ground surface (i.e., xoz plane) as the transceivers and the Ricker wavelet of 900MHz was used as the excitation signal. To emulate the operation of GPR system used for TBM applications, the dipole antennas were placed with orientations along the radii at different positions. GPR signals were acquired over eight concentric circles whose radii range from 0.15m to 0.5m with steps of 5cm and the azimuthal sampling intervals were 3° . Therefore, 960 spatial samples were obtained within the aperture in total but their polarizations varied at different azimuthal positions. For convenience, the parameters of GPR system and the media properties are summarized in Table II.

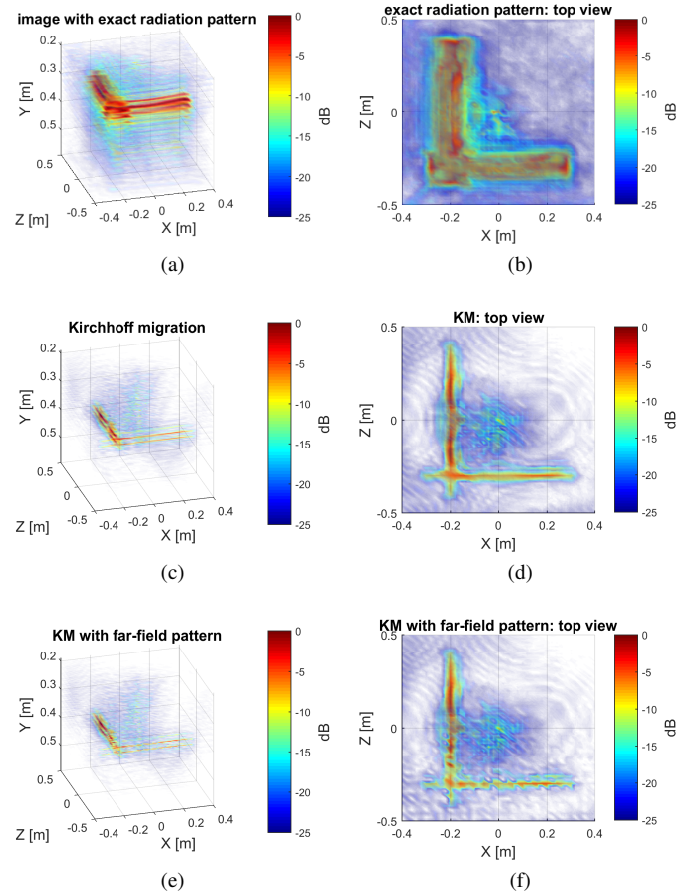


Fig. 4. Reconstructed images of cylinders buried in the soil with three different imaging approaches: (a), (c), and (e) are the 3-D images obtained by the linear inversion with exact radiation patterns, Kirchhoff migration, and Kirchhoff migration combining the far-field radiation patterns, respectively. (b), (d), and (f) are their corresponding top-view images.

After synthesizing the GPR data, the accurate Green's functions of rotated antennas at each position were computed over a $2 \times 2 \times 2$ cm volume grid with the suggested methods in the previous section. The relative permittivity of background soil $\epsilon = 9.0$ and conductivity $\sigma = 0$ were used for GF computation. The oversampling factor p was chosen to be four. Then the synthetic data were focused via the linear inversion method by considering the accurate radiation patterns of the antennas with varied polarizations at different positions (i.e., linear inversion with accurate radiation pattern, referred as LI-AccuRP below). In the implementation, the biconjugate gradients stabilized method (BiCGStab) was exploited to estimate the solution for the linear system of equations. For comparison, the Kirchhoff migration as well as the Kirchhoff migration combining the far-field approximation of the radiation patterns were also utilized for image formation. Integrating the far-field radiation pattern aims to correct the angle dependence of the dipole radiation which is generally neglected in the Kirchhoff migration. To avoid the blow-up of the signals after correction caused by the sharp minima in the far-field radiation patterns, only the signals that correspond to the radiation patterns down to -13dB with respect to its peak were compensated in the third imaging approach.

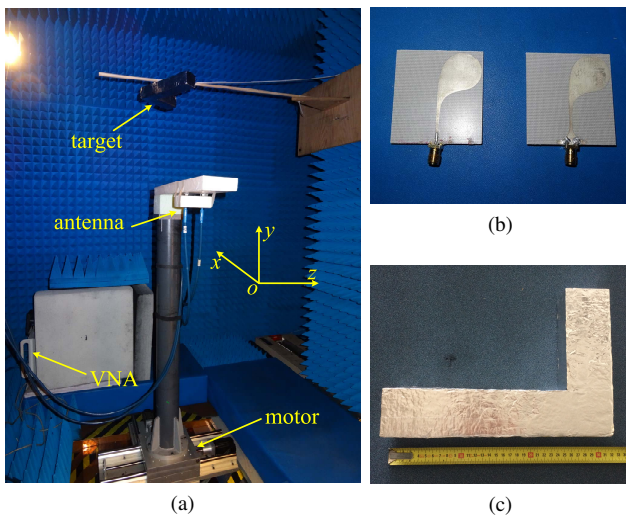


Fig. 5. The experimental measurement in anechoic chamber. (a) experimental setup, (b) antipodal Vivaldi antennas and (c) the “L”-shape target.

The images reconstructed with the three approaches are shown in Fig. 4, where all the images are normalized with respect to their own maximum absolute voxel values and shown in logarithmic scale for comparison. In all the images of Fig. 4 (a), (c) and (f), the “L” shape profiles of the joint cylinders are more or less reconstructed. However, in Fig. 4 (c) and (e) the reconstructed cylinders are much thinner than that in Fig. 4 (a). This is due to the striking angle dependence of the radiation patterns of the interfacial dipole antennas which significantly affects the strength of the signals observed from different aspects with respect to a target. Although the far field radiation patterns were employed to compensate the angle dependence of the observations in Fig. 4 (e) and (f), the resultant images are visually even worse than that without radiation pattern correction (Fig. 4 (c) and (d)). Specifically, the image of the cylinder parallel to the x -axis is fractured and in Fig. 4(f) the joint part of the two cylinders becomes dim compared to that in Fig. 4(d). This may result from the inadequate approximation of the far-field patterns in this case as well as the truncation effect on the radiation patterns for signal correction. In contrast to Fig. 4(c)–(f), the images formed with linear inversion are remarkably improved by accounting for the exact radiation patterns of dipole antennas (Fig. 4 (a) and (b)). Based on the Fig. 4(b), the diameters of the cylinders could be estimated although some artifacts are observed around the object. Note that the GFs used for imaging were computed by setting $\sigma = 0$, so they are not exact with respect to the real EM parameters of background soil. However, the reconstructed images are still dramatically improved compared to those obtained with traditional imaging approaches. Therefore, it shows the robustness of the proposed imaging approach.

V. EXPERIMENTS

As the rotated GPR instrument was unavailable, we instead took an experimental campaign in the anechoic chamber for imaging in free space.

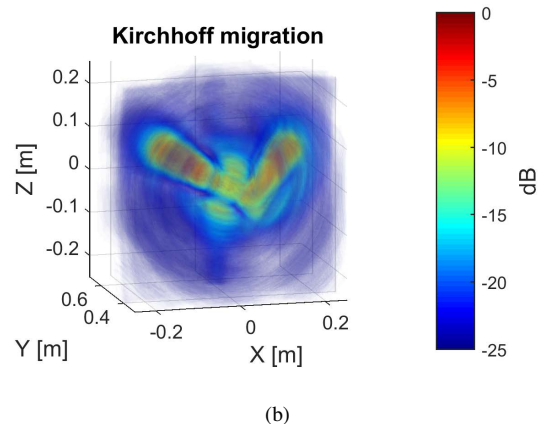
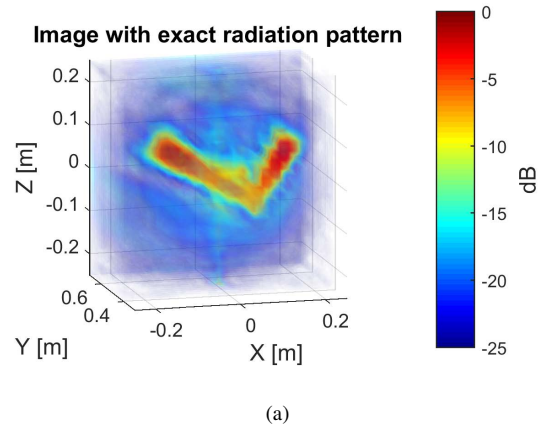


Fig. 6. Images of experimental measurements reconstructed by: (a) Linear inversion with accurate radiation pattern, (b) Kirchhoff migration.

A rotated experimental platform was built in the anechoic chamber in the TU Delft to emulate the signal acquisition for rotated arrays, as shown in Fig. 5 (a). Actually, this setup was similar to that we used in [7]. A column was installed on the base with the three-axis motion (i.e., two-axis translation and one-axis rotation), where a step motor was used to drive the base. On the top of the column, a polyethylene plastic panel was mounted as a support for the two Vivaldi antennas (see Fig. 5 (b)), i.e., one for transmitting and the other for receiving. Both Vivaldi antennas were connected to a vector network analyzer (VNA). By linear translation along the radius and the rotation along azimuth, a circular planar array was synthesized. An “L” shape object covered with aluminum foil was placed in front of the array at the distance of 0.5 m. The two arms of the “L” shape object are about 20 cm and 30 cm in length, respectively, 6 cm in width, and 5.5 cm in thickness (see Fig. 5 (c)). The spatial measurements were taken over some concentric circles with the radii ranging from 11 to 53 cm with steps of 3 cm. In azimuth, the sampling interval was 2.4° . The operational frequency of the VNA sweeps from 3 to 6 GHz with steps of 20 MHz.

To consider the direct coupling between the transmitter and the receiver and background reflections, the measurement was also performed with the absence of the object. After background subtraction, the signals reflected from the target were

obtained. Then the linear inversion approach with accurate radiation patterns was utilized to reconstruct the target's image from the frequency-domain signals. The reconstructed image is shown in Fig. 6 (a). Note that as the experimental measurement was conducted in free space, so the Green's functions for Hertz dipole in free space instead of half space were used for linear inversion [22]. For comparison, the signals after applying the inverse Fourier transform (IFT) to the measurements in the frequency domain were focused with Kirchhoff migration as well and the formed image is presented in Fig. 6 (b). Similar to the Fig. 4, the two images in Fig. 6 have been normalized with respect to their own maximum absolute voxel values and displayed in the logarithmic scale. From Fig. 6, one can see that both linear inversion with accurate radiation patterns and Kirchhoff migration acquire well-focused images of the target. However, the profile of the target is clearer and sharper in the image formed by linear inversion with accurate radiation pattern (Fig. 6 (a)) compared to that in the image focused by Kirchhoff migration (Fig. 6 (b)). Meanwhile, relatively larger artifacts and circularly sidelobes observed in Fig. 6 (b) are noticeably suppressed in Fig. 6 (a). Therefore, by considering the accurate radiation patterns of the rotated antenna arrays, improved images were obtained. As a consequence, in this case the computation time of the linear inversion approach (with 51 frequencies at each spatial position, i.e., the measurements were down-sampled every three frequencies) required ~ 350 s (about 340s for computing $\mathbf{D}^H \mathbf{D}$ in (8)) compared to the ~ 7 s of the Kirchhoff migration on a computer of 3.20 GHz CPU with four cores. The increase of computation time can be considered as a cost to be paid for the improved image quality. To accelerate the linear inversion approach, the matrix $\mathbf{D}^H \mathbf{D}$ can be precomputed and stored before the inversion operation, or more advanced inversion solvers should be exploited to circumvent the computation of $\mathbf{D}^H \mathbf{D}$.

Finally, we have to mention that although the "exact" GFs of the Hertz dipole are not exact with respect to the practical Vivaldi antenna, significant improvement is still observed in the reconstructed image with the suggested approach [see Fig. 6 (a)]. Again, it demonstrates the robustness of the suggested imaging approach.

VI. CONCLUSION

In this paper, we have presented a linear inversion approach for GPR systems with arbitrarily oriented transmit and receive antennas over data acquisition aperture. The approach models the wave propagation process with full-wave Green's functions and the image reconstruction is formulated as a linear inverse problem. Taking advantage of accurate Green's functions, the polarization and radiation pattern variations of GPR antennas within the aperture are taken into account and their effects are compensated during the imaging process.

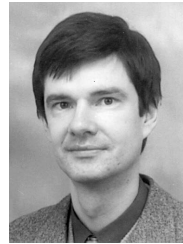
The focus of this paper is the construction of the observation matrix. In terms of the implementation of the proposed approach, computing the Green's functions with respect to each point in the scene is the key, yet the most computationally expensive step. To improve the computation efficiency, two methods are proposed for Green's function

calculation: interpolation-based method and Nonuniform Fast Fourier Transform (NUFFT) based method. Compared to the direct summation method, both methods significantly accelerate the Green's function computation and their accuracies were verified through numerical simulations. Besides for the imaging, these two efficient approaches for Green's function calculation can also benefit the investigation of the properties of the observation matrix for near-field imaging which is helpful to optimize the spatial signal sampling and imaging array design. It was shown in both simulations and measurements the proposed approach significantly improves the imaging performance (i.e., the sharpness of the focused image, artifacts suppression) compared to the traditional imaging algorithms such as scalar Kirchhoff migration and its combination with far-field radiation patterns. Especially, the method proposed is more suitable for reconstructing images of polarization independent subsurface objects and structures (such as point-like scatterers, spheres, and planar structures). The proposed approach can also be straightforwardly extended for full-polarimetric imaging when the signals are acquired with full-polarimetric antenna arrays.

REFERENCES

- [1] D. Daniels, *Ground Penetrating Radar, 2nd Edition*. Institution of Engineering and Technology, 2004.
- [2] T. Sato, K. Takeda, T. Nagamatsu, T. Wakayama, I. Kimura, and T. Shinbo, "Automatic signal processing of front monitor radar for tunneling machines," *Geoscience and Remote Sensing, IEEE Transactions on*, vol. 35, no. 2, pp. 354–359, 1997.
- [3] J. Wang, H. Cetinkaya, and A. Yarovoy, "On polar sampling of gpr for tunneling boring machine," in *Ground Penetrating Radar (GPR), 2014 15th International Conference on*, pp. 330–333.
- [4] J. Wang, H. Cetinkaya, A. Yarovoy, I. I. Vermesan, and S. Reynaud, "Investigation of forward-looking synthetic circular array for subsurface imaging in tunnel boring machine application," in *Advanced Ground Penetrating Radar (IWAGPR), 2015 8th International Workshop on*, pp. 1–4.
- [5] Z. Li, J. Wang, J. Wu, and Q. H. Liu, "A fast radial scanned near-field 3-D SAR imaging system and the reconstruction method," *Geoscience and Remote Sensing, IEEE Transactions on*, vol. 53, no. 3, pp. 1355–1363, 2015.
- [6] S. Zhu, W. Jian, L. Yu, S. Yi, and M. Sato, "A circular measurement for linearly polarized ground penetrating radar to map subsurface crossing cylinders," in *Geoscience and Remote Sensing Symposium (IGARSS), 2013 IEEE International*, pp. 1426–1429.
- [7] J. Wang, P. Aubry, and A. Yarovoy, "A novel approach to full-polarimetric short-range imaging with copolarized data," *IEEE Transactions on Antennas and Propagation*, vol. 64, no. 11, pp. 4733–4744, 2016.
- [8] J.-P. Van Gestel and P. L. Stoffa, "Migration using multiconfiguration gpr data," in *8th International Conference on Ground Penetrating Radar*. International Society for Optics and Photonics, 2000, pp. 448–452.
- [9] M. L. Moran, S. A. Arcone, and R. J. Greenfield, "Gpr radiation pattern effects on 3d kirchhoff array imaging," in *8th International Conference on Ground Penetrating Radar*. International Society for Optics and Photonics, 2000, pp. 208–212.
- [10] T. Wang and M. L. Oristaglio, "GPR imaging using the generalized radon transform," *GEOPHYSICS*, vol. 65, no. 5, pp. 1553–1559, 2000.
- [11] T. B. Hansen and P. M. Johansen, "Inversion scheme for ground penetrating radar that takes into account the planar air-soil interface," *Geoscience and Remote Sensing, IEEE Transactions on*, vol. 38, no. 1, pp. 496–506, 2000.
- [12] P. Meincke, "Linear GPR inversion for lossy soil and a planar air-soil interface," *Geoscience and Remote Sensing, IEEE Transactions on*, vol. 39, no. 12, pp. 2713–2721, 2001.
- [13] F. Lehmann, D. E. Boerner, K. Holliger, and A. G. Green, "Multicomponent georadar data: Some important implications for data acquisition and processing," *GEOPHYSICS*, vol. 65, no. 5, pp. 1542–1552, 2000.

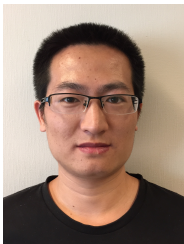
- [14] D. C. Nobes and A. P. Annan, "Broadside versus end-fire radar response: some simple illustrative examples," in *8th International Conference on Ground Penetrating Radar*. International Society for Optics and Photonics, 2000, pp. 696–701.
- [15] J. Kruk, C. Wapenaar, J. Fokkema, and P. van den Berg, "Three-dimensional imaging of multicomponent ground penetrating radar data," *GEOPHYSICS*, vol. 68, no. 4, pp. 1241–1254, 2003.
- [16] R. Streich and J. van der Kruk, "Accurate imaging of multicomponent GPR data based on exact radiation patterns," *Geoscience and Remote Sensing, IEEE Transactions on*, vol. 45, no. 1, pp. 93–103, 2007.
- [17] N. Engheta, C. H. Papas, and C. Elachi, "Radiation patterns of interfacial dipole antennas," *Radio Science*, vol. 17, no. 6, pp. 1557–1566, 1982.
- [18] H. van der Vorst, "Bi-cgstab: A fast and smoothly converging variant of bi-cg for the solution of nonsymmetric linear systems," *SIAM Journal on Scientific and Statistical Computing*, vol. 13, no. 2, pp. 631–644, 1992.
- [19] L. Greengard and J.-Y. Lee, "Accelerating the nonuniform fast fourier transform," *SIAM Review*, vol. 46, no. 3, pp. 443–454, 2004.
- [20] E. C. Slob, R. F. Bloemenkamp, and A. G. Yarovoy, "Efficient computation of the wavefield in a two media configuration emitted by a gpr system from incident field measurements in the air," in *Advanced Ground Penetrating Radar, 2003. Proceedings of the 2nd International Workshop on*, pp. 60–65.
- [21] C. Warren, A. Giannopoulos, and I. Giannakis, "An advanced gpr modelling framework: The next generation of gprmax," in *Advanced Ground Penetrating Radar (IWAGPR), 2015 8th International Workshop on*, July 2015, pp. 1–4.
- [22] C.-T. Tai, *Dyadic Green's functions in electromagnetic theory*, ser. The Intext monograph series in electrical engineering. Scranton: Intext Educational Publishers, 1971.



Alexander Yarovoy (F'15) received the Diploma (with honor) in radiophysics and electronics in 1984, and the Candidate Phys. & Math. Sci. and Doctor Phys. & Math. Sci. degrees in radiophysics in 1987 and 1994, respectively, all from the Kharkov State University, Kharkov, Ukraine.

In 1987, he joined the Department of Radiophysics at the Kharkov State University as a Researcher and became a Professor there in 1997. From September 1994 to 1996, he was with the Technical University of Ilmenau, Ilmenau, Germany, as a Visiting Researcher. Since 1999, he has been with the Delft University of Technology, Delft, The Netherlands. Since 2009, he leads there as the Chair of Microwave Sensing, Signals and Systems. His main research interests are in ultrawideband microwave technology and its applications (particularly radars) and applied electromagnetics (particularly UWB antennas). He has authored and coauthored more than 250 scientific or technical papers, four patents, and 14 book chapters.

Prof. Yarovoy served as a Guest Editor of five special issues of the IEEE Transactions and other journals. Since 2011, he has been an Associated Editor of the International Journal of Microwave and Wireless Technologies. He is the recipient of the European Microwave Week Radar Award for the paper that best advances the state of the art in radar technology in 2001 (together with L. P. Ligthart and P. van Genderen) and in 2012 (together with T. Savelyev). In 2010, together with D. Caratelli, he got the best paper award of the Applied Computational Electromagnetic Society (ACES). He served as the Chair and TPC Chair of the 5th European Radar Conference (EuRAD 08), Amsterdam, The Netherlands, as well as the Secretary of the 1st European Radar Conference (EuRAD 04), Amsterdam. He served also as the Cochair and TPC Chair of the Xth International Conference on Ground Penetrating Radar (GPR 2004) in Delft, The Netherlands. Since 2008, he has served as the Director of the European Microwave Association.



Jianping Wang received BSc. degree from North China University of Technology in 2009 and MSc. degree from Beijing Institute of Technology, Beijing, China, in 2012, both in electrical engineering.

From August, 2012 till April, 2013, he worked as a research associate in the University of New South Wales (UNSW), Australia, on FMCW SAR signal processing for formation flying satellites. In 2013, He joined the group of Microwave Sensing, Signals and Systems (MS3) in the Delft University of Technology, Delft, the Netherlands, where he is

working towards the PhD degree. His research interests include radar imaging, signal processing, and antenna array design.



Pascal Aubry received the D.E.S.S. degree in electronics and automatics from the Universit Pierre et Marie Curie (Paris 6), Paris, France, in 1993.

He was a Young Graduate Trainee with the European Space Research and Technology Centre (ESTEC) in 1996, where he was involved in antenna measurements. Since 1997, he has been with the International Research Centre for Telecommunications and Radar, Delft University of Technology (TUD), Delft, The Netherlands. His research interests include antenna measurement techniques, radar system

testing, and signal processing and analysis.